2-D soft x-ray arrays in the EAST

Kaiyun Chen, Liqing Xu' , Liqun Hu, Yanmin Duan, Xueqin Li, Yi Yuan, Songtao Mao, Xiuli Sheng, and Jinlong Zhao

Citation: Review of Scientific Instruments **87**, 063504 (2016); doi: 10.1063/1.4953837
View online: http://dx.doi.org/10.1063/1.4953837
View Table of Contents: http://aip.scitation.org/toc/rsi/87/6
Published by the American Institute of Physics

2-D soft x-ray arrays in the EAST

Kaiyun Chen,[1] Liqing Xu,[1,a)] Liqun Hu,[1] Yanmin Duan,[1] Xueqin Li,[2] Yi Yuan,[1] Songtao Mao,[1] Xiuli Sheng,[1] and Jinlong Zhao[1]
[1]*Institute of Plasma Physics, Chinese Academy of Sciences, Hefei 230031, China*
[2]*Hefei Juneng Electro Physics, Hefei 230031, China*

(Received 3 December 2015; accepted 1 June 2016; published online 17 June 2016)

A high spatial and temporal resolution soft x-ray (SXR) imaging diagnostic has been installed in EAST for the study of magnetohydrodynamics activities and core high-Z impurity transport. Up to 122 lines of sight view the poloidal plasma from three directions (two up-down symmetrical horizontal arrays and one vertical array), which renders the diagnostic able to provide detailed tomographic reconstructions under various conditions. Fourier-Bessel method based on flux coordinates was employed for 2-D SXR tomographic reconstruction. Examples of several events measured by SXR diagnostic in EAST are shown, namely the crash patterns of sawtooth, periodical burst of edge localized modes, and the transport of high-Z intrinsic impurities. *Published by AIP Publishing.* [http://dx.doi.org/10.1063/1.4953837]

I. INTRODUCTION

SXR multi-arrays, 2-D electron cyclotron emission imaging (ECEI), edge Mirnov coils (MC), and 1-D ECE are standard diagnostic instruments on tokamaks for magnetohydrodynamics (MHD) study. However, apart from SXR diagnostic, other diagnostics have certain limitations for the study of large scale core MHD phenomena. MC directly measured the magnetic fluctuations, however, MC cannot give the spatial structure of MHD. ECE can provide well resolved radial structure, however, the poloidal and toroidal mode numbers must be known[1] and ECEI cannot obtain the whole structure of large MHD due to the limitation of small radial space available. Therefore, a high spatial and temporal resolution SXR is the most suitable for MHD measurement.[2–5] In addition, SXR emission from tokamak plasmas is dependent on various plasma parameters, such as density, temperature, and impurity, and one can infer information about them by observing this radiation.[6–8] This information can also be analyzed and related to properties such as plasma position shape and impurity distribution. Thus, SXR arrays have become standard diagnostic equipment on tokamaks.[2–8]

SXR signal is line-integrated. However, to better illustrate MHD activities, it is highly favorable to have as much knowledge of the spatial structure of the soft x-ray emissivity as possible. Therefore, 1-D SXR chord mapping to plasma equilibrium and 2-D SXR tomographic reconstruction are necessary in data analysis.[9–12]

The 2-D soft X-ray arrays system presented in this paper was installed on EAST tokamak. EAST is a medium sized, divertor configuration tokamak with a major radius $R_0 = 1.75$ m and minor radius a = 0.45 m. The toroidal magnetic field B_T = 1.6–2.5 T in clockwise and plasma current Ip = 200–600 kA in counter-clockwise direction.[13]

In this paper, a 3-array SXR diagnostic with a spatial resolution about 2.5 cm and a temporal resolution up to 10 μs is described. 1-D SXR perturbation profile, associated with MHD oscillations, based on chord tangency is presented. Also, 2-D SXR tomography, measured by SXR multi-array, developed from Fourier-Bessel method is discussed. The remainder of this paper is organized as follows: Sec. II describes the layout of SXR system. In Sec. III, the mapping of chord tangency to EFIT based flux coordinates is presented. 2-D SXR tomographic reconstruction is given in Sec. IV. In Sec. V, we present some EAST SXR data. Finally, we summarize our main points in Sec. VI.

II. SOFT X-RAY CAMERA SYSTEM

The energy spectrum of soft X-ray radiation consists of a continuum of free-free bremsstrahlung, free-bound recombination radiation, and bound-bound line radiation. Continuum radiation arises from electron-ion collisions and from recombination. Line radiation is a result of transition in an ion from one to another excitation state, which can also occur when a recombination process leaves an ion in an excited state.[6–8]

A. Detectors

The detectors inside the cameras in EAST SXR diagnostic are Hamamatsu Si photodiode arrays S4114 series (S4114-46Q). This is a linear array of 46 diodes on a single silicon chip. The geometrical parameters of the diodes are the following: diode width $D_x = 0.9$ mm, diode length $D_y = 4.4$ mm, separation between elements measure $L_{free} = 0.1$ mm, separation between elements pitch $L_{element} = 1.0$ mm, and diode effective $S_D = 3.96$ mm^2. The diodes are connected unbiased. Three diodes are not absolutely calibration, but a cross-calibration of 3 arrays is done via MHD-IC code.[14]

a)E-Mail: lqxu@ipp.cas.cn

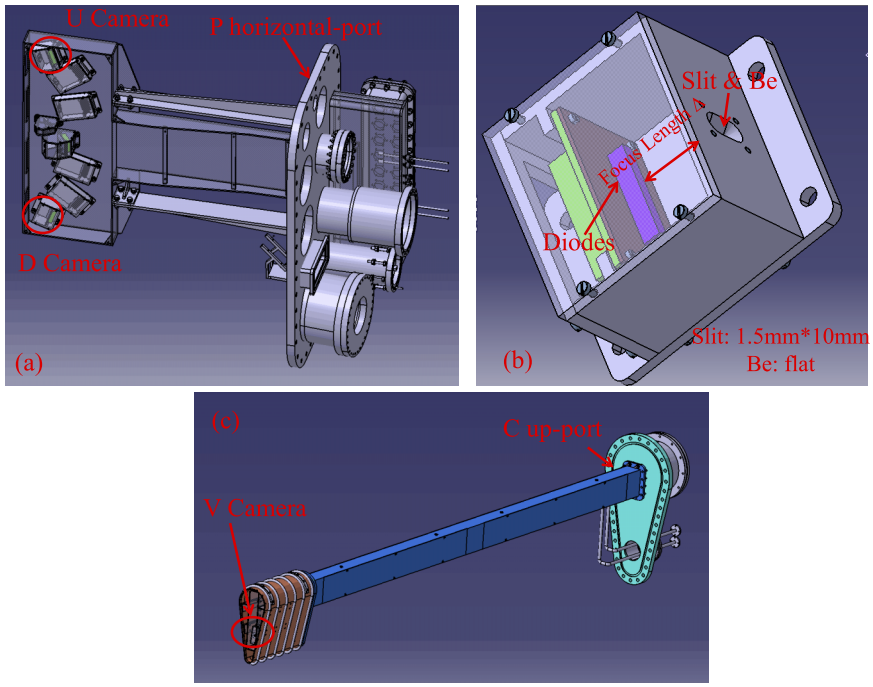

FIG. 1. (a) Schematic view of the SXR cameras (U and D) installed in EAST. (b) Sketch of the SXR head and (c) V camera in EAST C-up port.

B. Pinhole cameras

The current SXR system at EAST consists of 3 cameras all having one head. Each head contains one diode array (S4114-46Q) and has its own pinhole and beryllium filter foil. The pinhole centre corresponds to the middle of the diode array. The flat Be thickness of the all three cameras, named U, D and V, is 12.5 μm. The size of all three slits is 1.5 mm $\times$ 10 mm. The focal length (Δ), distance from pinhole to the centre of diode array is 40 mm, 40 mm, and 81 mm for U, D and V cameras, respectively. Finite beam width effect, Be-foil attenuation effect, and Be -foil thickness error have been considered in the EAST image reconstruction routine. It is found that finite beam width effect hardly influences the reconstruction results, whereas Be-foil thickness error can lead to severe noise in the reconstructed image. The thickness error of Be is less than 0.5 μm. Figures 1(a) and 1(c) show the schematic of U, D cameras in EAST P horizontal port and V camera in EAST C vertical port, respectively. The details of SXR head are presented in Figure 1(b). The iron box of the head was used for magnetic shielding.

C. Position of the cameras

As shown in Figure 2, EAST is equipped with 2 cameras in horizontal port P and one camera in vertical port C. The two horizontal cameras, U and D cameras, in port P are located in different poloidal but almost at the same toroidal position. The vertical camera V in port C is 67.5° toroidally separated from U and D arrays. Cameras U and D are up-down symmetrical in poloidal section, both of them have 46 view lines which cover the whole plasma region. The position of pinhole (P_x, P_y) of U and D is (2.85 m, 0.3326 m) and (2.85 m, −0.3326 m) in (R, Z) plane. The angles (α) of U and D are 19.43° and −19.43°, respectively. Here the camera angle (α) is the angle of the chip normal with respect to the horizontal line pointing outward in counterclock wise direction. Due to the space limitation, the camera V only has 30 lines, and only covers the lower field side. The position of pinhole(P_x, P_y) of V is (1.8503 m, 1.4402 m). The angle (α) of V is 98°. The positions of all cameras and lines of sight are shown in Figure 2. The position of cameras is measured by a robot arm after they are installed on a vacuum chamber.

D. Data acquisition system

The main components of the acquisition system for a particular line of sight are shown in Figure 3. The current from the diode is converted into voltage and amplified by a

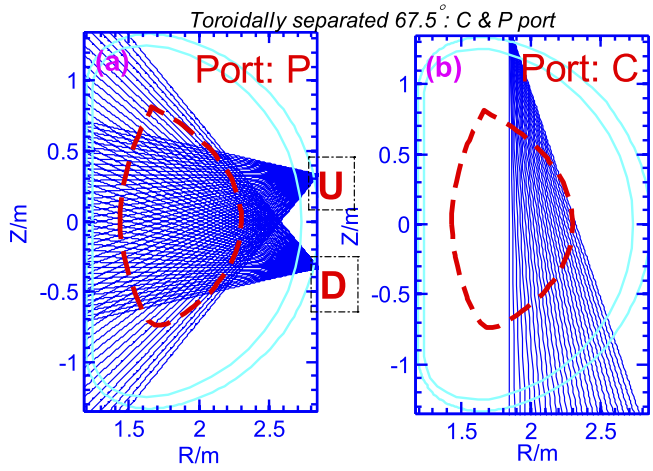

FIG. 2. Shown is the projection of the soft X-ray lines of sight to the poloidal cross-section, in which the camera pinhole is located. U and D cameras are located in port P and V in port C. The red dotted circle is the EAST typical last closed flux surface.

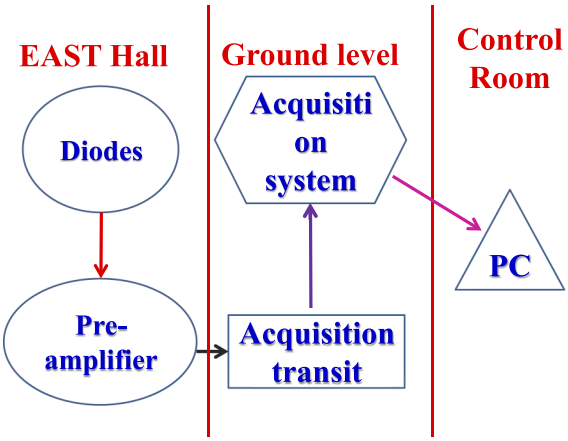

FIG. 3. Scheme of the soft X-ray data acquisition system is shown.

preamplifier mounted close to the torus. The amplifiers contain the analog-to-digital converter (ADC). In the preamplifiers the diode dark currents are compensated and then shifted by a fixed offset before the discharge. Thus the signals without detected radiation are close—but not quite at—the zero level of the ADC. This allows to have a large data range independent of the dark current and still to see the full noise level of the signals even without radiation. There are three types of amplification factors of preamplifiers, 4×10^5, 5×10^5, and 2×10^6. The amplification factor can be easily changed between different discharges depending on the discharge condition. From amplifier devices, the data are first sent to an acquisition transit cabinet, which is located in the ground level of EAST hall, before being uploaded to the EAST uniform diagnostic acquisition system. Finally, the user can find the SXR data from EAST data servers by personal computer.

The soft X-ray diagnostic is equipped with 126 channel ADCs and has a 100 kHz sampling rate. The observed frequency range (up to 50 kHz) is sufficient for the investigation of standard MHD instabilities (sawtooth precursors, tearing modes, fishbones, etc.).

III. MAPPING LINE-INTEGRATED SXR SIGNAL TO EFIT

For the non-circular elongated plasma, a chord tangency parameter was employed for representation of SXR integrated line instead of using impact parameter for circular plasma. The equilibrium poloidal flux Ψ was real-time calculated by EFIT code. All the SXR chord tangency points (lines tangency to Ψ) are then mapped to the EFIT equilibrium in PEST straight field line coordinate.[15] A normalized poloidal flux radius ρ, with $\rho = \sqrt{\frac{\Psi-\Psi_a}{\Psi_s-\Psi_a}}$ (where Ψ is the poloidal flux, and the indices s and a refer to the seperatrix and magnetic axis, respectively) is chosen.

IV. 2-D TOMOGRAPHIC RECONSTRUCTION

In EAST, we have developed many kinds of image reconstruction routines, including maximum entropy technology,[16–19] minimum Fisher information technology,[10,20] constrained optimization method,[11,12] and Fourier-Bessel method.[17] By comparing these algorithms, it is found that Fourier-Bessel analytical method is best suited for the EAST soft X-ray reconstruction because the reconstruction was only focused on the bulk plasma region and m = 1 MHD core mode. The soft X-ray tomography combines the signals from all U, D, and V camera sight lines to reconstruct a poloidal cross section of total emissivity (or perturbation of the emissivity). The Fourier-Bessel inversion method is used in the reconstruction by choosing M = 1–2 and L = 7. The local emissivity can be expanded in terms of Fourier harmonics to yield

$$g(r,\theta^*) = \sum_{m=0}^{M} [g_m^c(\rho)\cos(m\theta^*) + g_m^s(\rho)\sin(m\theta^*)].$$

Expanded $g_m(r)$ as terms of Bessel series and the chord brightness f can be written as

$$f = \sum_{m=0}^{M}\sum_{l=0}^{L}\int_L [a_{ml}^c(\rho)\cos(m\theta^*) + a_{ml}^s(\rho)\sin(m\theta^*)]J_m(\lambda_m^{l+1}\rho)dL,$$

where λ_m^{l+1} is the lth zero of the Bessel function, θ^* is angular orientation in PEST coordinate. Note that an aero boundary condition and positive SXR emission are used for Fourier-Bessel tomography as compulsive restrictions.[5]

In order to obtain the picture of mode reconstruction, the singular value decomposition technology (SVD) technique is employed to extract the perturbation components from the total signals.[10] SVD method is also used for the cross-calibrated U, D, and V arrays. The toroidal rotation direction of mode and the mode numbers (m/n, m-poloidal, n-toroidal) should firstly be addressed by assistance of edge vacuum chamber located and toroidally equal spaced MC, before tomography combines U, D in P port and V in C port, because of the different toroidal position between U, D and V cameras. A same method was used at JET due to the same issue of toroidally separated SXR cameras.[21]

Shown in Figure 4(a) is the example of 1/1 ideal kink mode *snake* radial structure. The *snake* is extracted from the

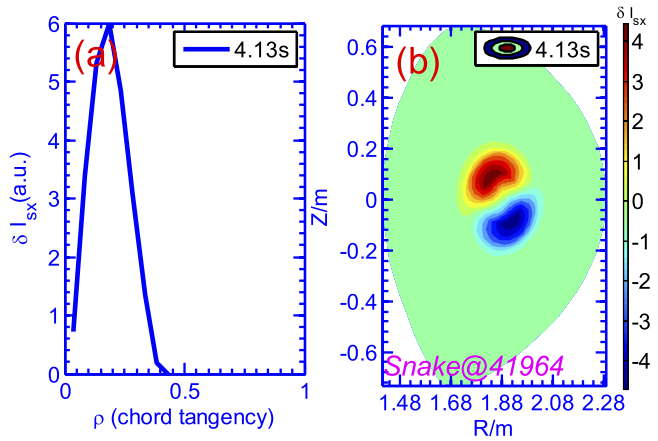

FIG. 4. Spatial structure of 1/1 ideal kink mode measured by SXR imaging. (a) Measured line-integrated U-SXR emission amplitude plotted versus chord tangency ρ, (b) 2-D structure via tomographic reconstructions, the background radiation was subtracted via SVD.

total emission of camera U by SVD. *snakes* in EAST shot No. 41964 were located in the plasma core region at $\rho = 0.2$. The *snakes* 2-D perturbation structure was obtained by SXR tomography,[16–19] as shown in Figure 4(b).

V. EXPERIMENTAL DATA

The current SXR diagnostic works well in EAST 2014 and 2015 campaign. In this section, a series fo events will be given for example, which namely are the crash patterns of sawtooth, periodic burst of edge localized modes, and the transport of high-Z intrinsic impurities.

A. Sawtooth crash and 1/1 kink mode

The sawtooth phenomena commonly observed in the tokamak plasmas are periodic relaxation events characterized by fast collapse of the heat slowly accumulated in the core region. Typical sawtooth cycle consists of three phases: quiescent ramp up phase, oscillation phase, and fast collapse phase, as shown in Figure 5. SXR profile becomes more and more peaked during the ramp phase, which reflects the shrinkage of plasma current and pressure profile, as illustrated in the tomographic patterns A–C in Figure 5. The peaked current profile then triggers 1/1 kink mode and the following fast growth of 1/1 mode finally leads to a crash of the sawtooth.

Nearly circular SXR core (Figure 5, pattern D) resembles the 1/1 oscillation before sawtooth crash with ideal kink mode nature. The SXR profile formation becomes slightly hollow during the sawtooth crash phase, as seen in the SXR raw profiles at the second and third column of the upper row in Figure 5 and also in pattern E of Figure 5. A considerable heat flow transferring outside is also observed during the sawtooth crash (Figure 5) (note that there is no high-Z impurity accumulation during sawtooth crash). After the sawtooth crash, the broad SXR hot core recovers before the next sawtooth cycle (Figure 5, pattern F).

B. Edge localized mode

During the formation of the pedestal in high confinement plasma, the increase of plasma density and temperature gradients leads to a substantial gain in energy and fusion performance. However pressure pedestal, may cause edge MHD instabilities, such as edge-localized modes (ELMs), when reaching a critical limit. Crude bursts of ELMs lead to transient high heat load greatly which may exceed the thermal load capacity of plasma facing materials. Therefore, the study and control of ELMs are vital to achieve better tokamak operation. SXR array V covering the lower field side in EAST

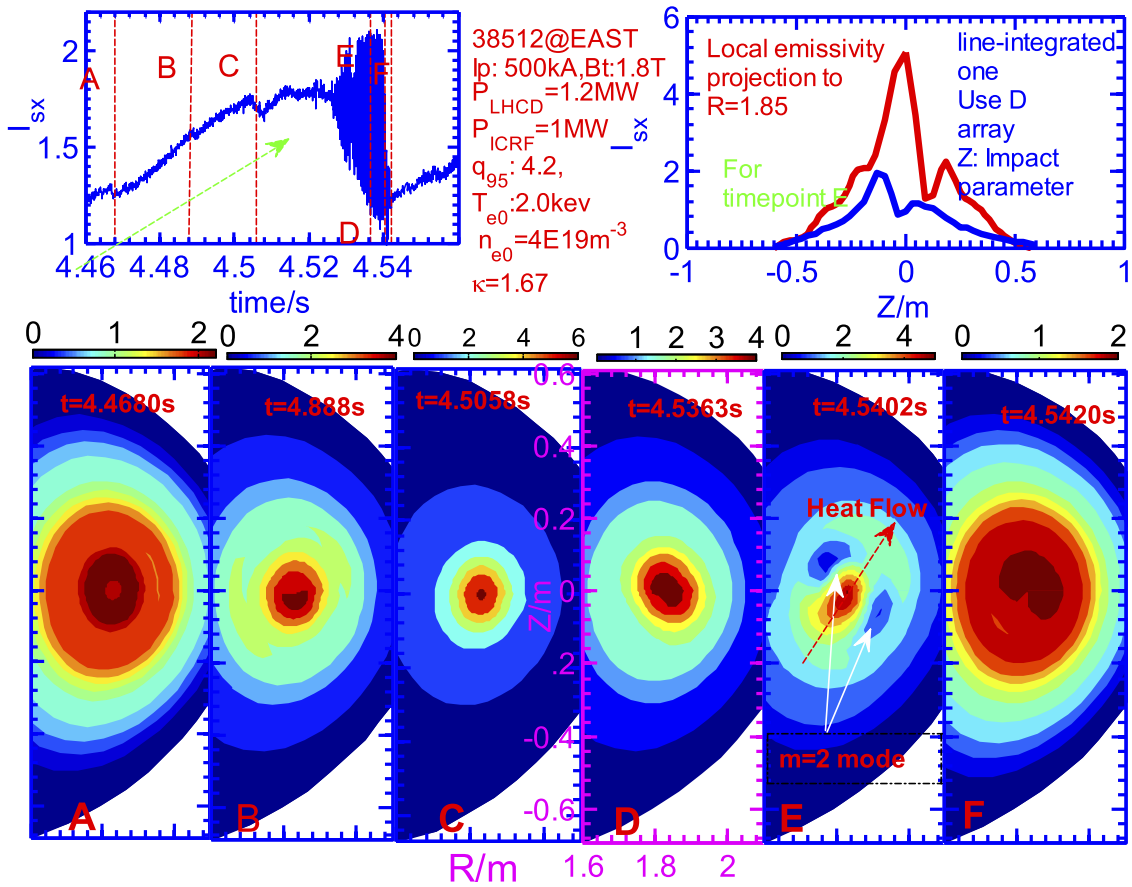

FIG. 5. Typical 2-D sawtooth patterns measured by SXR imaging in EAST. The top row shows the evolution of the line-integrated soft-x-ray signals at central chord (left) and the profiles of D camera at time E, blue line is the raw line-integrated data and red is the reconstructed local data projection to R = 1.85 m. The bottom row is the contour plot of the reconstructed local emission intensity profiles from the total signals. The capital letters on the left of the reconstructed frames correspond to those in the top row left frame.

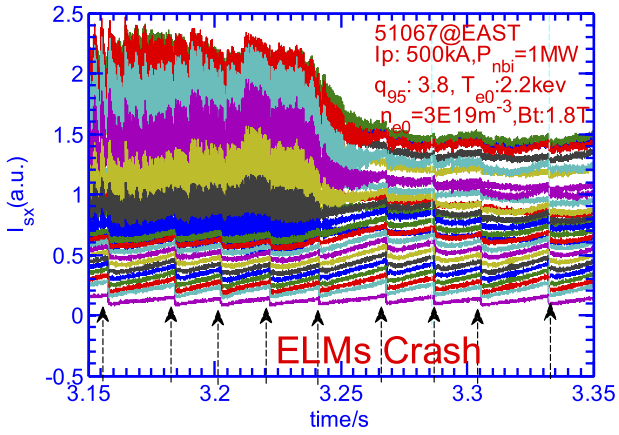

FIG. 6. Example of fast edge localized mode measured by V camera. The arrows indicate the crash of ELMs.

is a efficient tool to the ELMs structure and real-time control study.

Shown in the Figure 6 is the fast ELMs crash picture captured by SXR V camera. The periodic ELMs resemble sawtooth crash in their form but have a radial structure with no inversion in the whole region. Sawtooth-like crashes are seen in all the V camera viewing lines, but with all strong amplitude scale crashes occurring only in the edge chords, it is safe to assume that ELMs occur at plasma edge.

C. Core high-Z impurity transport

Tungsten (W) or molybdenum (Mo) is well suited to serve as materials for plasma facing components in terms of their thermal load capability, low erosion yield, and low deuterium retention.[6] However, when the W, Mo, or the other intrinsic impurity (e.g., Fe, Cu from antennas) concentration exceeds a certain level in the central part of the plasma the radiative losses would limit the plasma operation. A combination of fast SXR and EUV spectrometer can give the fast evolution of concentration of high-Z impurities, hence the impurity cooling factor and effective ionic charge (Z_{eff}).[6–8]

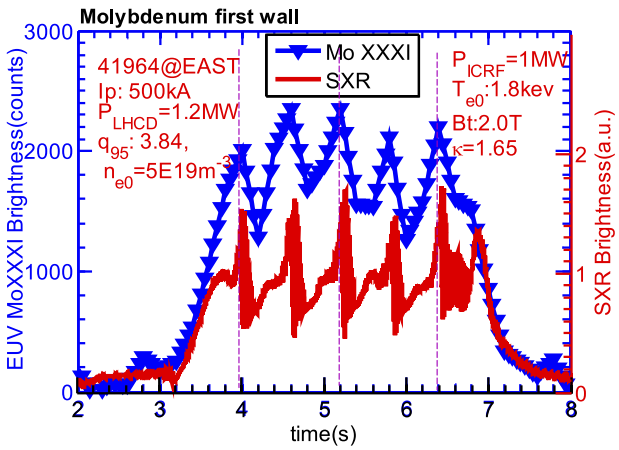

FIG. 7. Comparison between SXR emission and intrinsic high-Z impurity intensity measured by extreme ultraviolet spectrometer. Good agreement between SXR and EUV is found.

In EAST, core impurity-related snake mode is studied by applying both of SXR and EUV.[22,23] A space-resolved EUV spectrometer covers a wavelength range of 5-50 nm. The obtained best time resolution is 25 ms and with entrance slit height at 1 mm the spatial resolution has reached 45 mm.[23] A massive Mo transport to the plasma core region is occasionally found in 4.6 GHz lower hybrid current drive H mode plasma by the monitoring of EUV or SXR signals. Figure 7 shows a typical Mo transport to the plasma core. Good agreement between SXR and EUV is found. Here, we took both the EUV and SXR signals at Z = 0.

VI. SUMMARY AND FUTURE PLANS

The EAST SXR diode array was first installed in 2007, the configuration changes from time to time, and the current SXR diagnostic has three operating cameras. The routine data analysis including both 1-D chord mapping and 2-D tomographic reconstruction of SXR is detailed in this paper. Examples of 2-D picture of sawtooth crash, evolution of ELMs as well as high-Z impurity transport are also presented.

In order to achieve 2-D measurement of higher mode number MHD (e.g., 3/2 mode and ELMs), we plan to add one more vertical array to view the poloidal plasma cross-section from the bottom port. Guiding by the impurity cooling factor measurement, absolute calibration of SXR power is also under consideration. High sampling rate ADCs and fast data acquisition of SXR system are urgently needed for high frequency energy particle-related mode study.

ACKNOWLEDGMENTS

We are grateful to Dr. Yongcai Shen at ASIPP for providing EUV data and Professor Youwen Sun for providing flux coordinate mapping code. This work was partially supported by the JSPS-NRF-NSFCA3 Foresight Program in the field of Plasma Physics under Contract No. 11261140328, the National Nature Science Foundation of China under Contract No.11505226.

[1]M. Sertoli, L. Horvath, G. Pokol, V. Igochine, L. Barrera, and ASDEX Upgrade Team, Nucl. Fusion **53**, 053015 (2013).
[2]L. Ingesson, B. Alper, B. Peterson, and J. Vallet, Fusion Sci. Technol. **53**, 528–576 (2008).
[3]Q. Xiao and G. Navratil, Rev. Sci. Instrum. **67**, 3334 (1996).
[4]S. V. Goeler, R. Kaita, M. Bitter, G. Funchs, M. Poier, G. Bertschinger, H. R. Koslowski, F. Toi, S. Ohdachi, and A. Donne, Rev. Sci. Instrum. **70**, 599 (1999).
[5]B. Alper, S. Dillon, A. W. Edwards, R. D. Gill, R. Robins, and D. J. Wilson, Rev. Sci. Instrum. **68**, 778 (1997).
[6]T. Putterich, R. Dux, R. Neu, M. Bernert, M. N. A. Beurskens, V. Bobkov, S. Brezinsek, C. Challis, J. W. Coenen, and I. Coffey, Plasma Phys. Controlled Fusion **55**, 124036 (2013).
[7]M. Sertoli, R. Dux, T. Putterich, and ASDEX Upgrade Team, Plasma Phys. Controlled Fusion **57**, 075004 (2015).
[8]M. Galante, L. Reusch, H. D. Den, P. Franz, J. Johnson, M. McGarry, M. Nornberg, and H. Stephens, Nucl. Fusion **55**, 123016 (2015).
[9]D. Mazon, D. Vezinet, D. Pacella, D. Moreau, L. Gabelieri, A. Romano, P. Malard, J. Mlynar, R. Masset, and P. Lotte, Rev. Sci. Instrum. **83**, 063505 (2012).
[10]M. Anton, H. Weisen, M. J. Dutch, W. Von der Linden, F. Buhlmann, R. Chavan, B. Marletaz, P. Marmillod, and P. Paris, Plasma Phys. Controlled Fusion **38**, 1849 (1996).

[11]R. S. Granetz and P. Smeulders, Nucl. Fusion **28**, 457 (1988).
[12]L. C. Ingesson, B. Alper, H. Chen, A. W. Edwards, G. C. Fehmers, J. C. Fuchs, R. Giannella, R. D. Gill, L. Lauro-taroni, and M. Romanelli, Nucl. Fusion **38**, 1675 (1998).
[13]B. Wan, J. Li, H. Guo, Y. Liang, G. Xu, L. Wang, X. Gong, and Andrea Garofalo for the EAST Team and Collaborators, Nucl. Fusion **55**, 104015 (2015).
[14]V. Igochine, S. Gunter, M. Maraschek, and ASDEX Upgrade Team, Nucl. Fusion **43**, 1801 (2003).
[15]R. Grimm, R. Dewar, and J. Manickam, J. Comput. Phys. **49**, 94–117 (1983).
[16]P. Smeulders, "A fast plasma tomography routine with second-order accuracy and compensation for spatial resolution," Max-Planck-Institut fur Plasmaphysik, IPP 2/252, 1983.
[17]Y. Nagayama, Rev. Sci. Instrum. **65**, 3415–3422 (1994).
[18]H. Krause, M. Kornherr, ASDEX Team, and NI Team, "High resolution sparse channel tomography for slowly varying rotating SXR profiles," in *15th European Conference on Controlled Fusion and Plasma Heating, Contributed Papers* (European Physical Society, Geneva, 1988), pp. 1179–1182, http://hdl.handle.net/11858/00-001M-0000-0029-0E3A-9.
[19]R. Buchse, "Tomographische Untersuchung interner Disruptionen an den Tokamaks ASDEX und TFTR," Max-Planck-Institut fur Plasmaphysik, IPP III/175, 1991.
[20]V. Loffelmann, J. Mlynar, M. Imrisek, D. Mazon, A. Jardin, V. Weinzettl, and M. Hron, Fusion Sci. Technol. **69**, 505 (2016).
[21]J. Mlynar, M. Odstrcil, M. Imrisek, B. Alper, A. Murari, and JET EFDA Contributors, "2D tomography of SXR data from toroidally separated cameras for studies of impurity injection and fast instabilities on JET," in *38th EPS Conference on Plasma Physics*, P 4.052 (2011).
[22]L. Xu, L. Hu, K. CHen, C. Li, E. Li, J. Zhao, X. Sheng, J. Zhang, and S. Mao, Chin. Phys. Lett. **31**, 105201 (2014).
[23]Y. Shen, X. Du, W. Zhang, Q. Wang, Y. Li, J. Fu, F. Wang, J. Xu, B. Lu, Y. Shi, and B. Wan, Nucl. Instrum. Methods Phys. Res., Sect. A **700**, 86–90 (2013).